Acoustic Wave Guiding by Reconfigurable Tessellated Arrays

Chengzhe Zou, Danielle T. Lynd, and Ryan L. Harne*
Department of Mechanical and Aerospace Engineering, The Ohio State University, Columbus, Ohio 43210, USA

(Received 27 September 2017; revised manuscript received 13 November 2017; published 10 January 2018)

The reconfiguration of origami tessellations is a prime vehicle to harness for adapting system properties governed by a structural form. While the knowledge of mechanical property changes associated with origami tessellation folding has been extensively built up, the opportunities to integrate other physics into a framework of tessellated, adaptive structures remain to be fully exploited. Acoustics appears to be a prime domain to marry with origami science. Specifically, deep technical analogies are revealed between wave-guiding properties achieved via digital methods that virtually reposition array elements and the actual repositioning of facets by folding origami-inspired tessellations. Here we capitalize on this analogy to investigate acoustic arrays established upon facet layouts of origami-inspired tessellations. We show that a concept of reconfigurable tessellated arrays may guide waves more effectively than traditional digitally phased arrays using fewer transducer elements. Moreover, we show that the refinement of tessellated arrays trends to the ideal case of classical wave radiators or receivers grounded in principles of geometrical acoustics. By linear wave physics shared among myriad scientific disciplines and across orders of magnitude in length scale, these discoveries may cultivate numerous opportunities for wave-guiding adaptive structures inspired by low-dimensional origami tessellations.

DOI: 10.1103/PhysRevApplied.9.014009

I. INTRODUCTION

Investigations on the composition, reconfiguration, and mechanics of origami-based structures [1] have recently established broad theoretical foundations for the study and development of shape-adaptable metamaterials [2–4], programmable structures [5–7], and bistable and multistable systems [8–10]. Nevertheless, these contexts take advantage of only the topological and mechanical characteristics of origami architectures. The potential for the principles of origami to advance other physical disciplines remains an area of exploration. To this end, frequency-selective antenna [11,12], foldable lenses [13,14], tunable equivalent media [15,16], and thermally driven origami structures [17] are prime examples where shape changes are leveraged to tailor topologically governed properties. Here this report finds that the intersection between wave physics and origami-inspired design is a prime opportunity whereby tessellated structures use shape reconfiguration to tailor wave-guiding properties.

Acoustic wave guiding is commonly achieved by the virtual repositioning of transducer elements in arrays via digital beam-forming techniques [18]. In these techniques, phase delays and amplitude weights are used for elements of an assembled array [Fig. 1(a)]. The computational burden, cost, and implementation may become exacerbated, because a sufficiently great number of elements is needed to authoritatively guide wave energy by digital methods [19–21]. Yet, the repositioning of facets is actually achieved by folding, tessellated structures [Fig. 1(a)]. Compared with digital methods that independently control each array element, the actual repositioning of transducer elements enabled by an array established on an origami tessellation architecture may be more straightforward by way of the low degree-of-freedom folding actions. In addition, the foldability of a tessellated array cultivates unique portability for arrays that must be transported and deployed for use [22,23], such as for *in vivo* ultrasound therapy. Motivated by these potentials, our previous work explored adaptive acoustic wave guiding enabled by this concept [24–26], and the outcomes have qualitatively verified its feasibility as an alternative to conventional digital wave-guiding methods.

Yet, there remains no quantitative comparison between virtual and actual repositioning of elements achieved, respectively, by digital beam-forming and tessellated arrays, which prevents a detailed characterization of the contrast of methods. This report addresses the lack of knowledge by revealing the origins of wave guiding achieved through foldable arrays as contrasted to conventional phased arrays. As a result, potential pathways to integrate such methods for wave-guiding properties with exceptional wave guiding and straightforward implementation are illuminated. This insight could impact applications representing orders of magnitude in scale where digital controls are used to guide wave radiation and reception

*Corresponding author.
harne.3@osu.edu

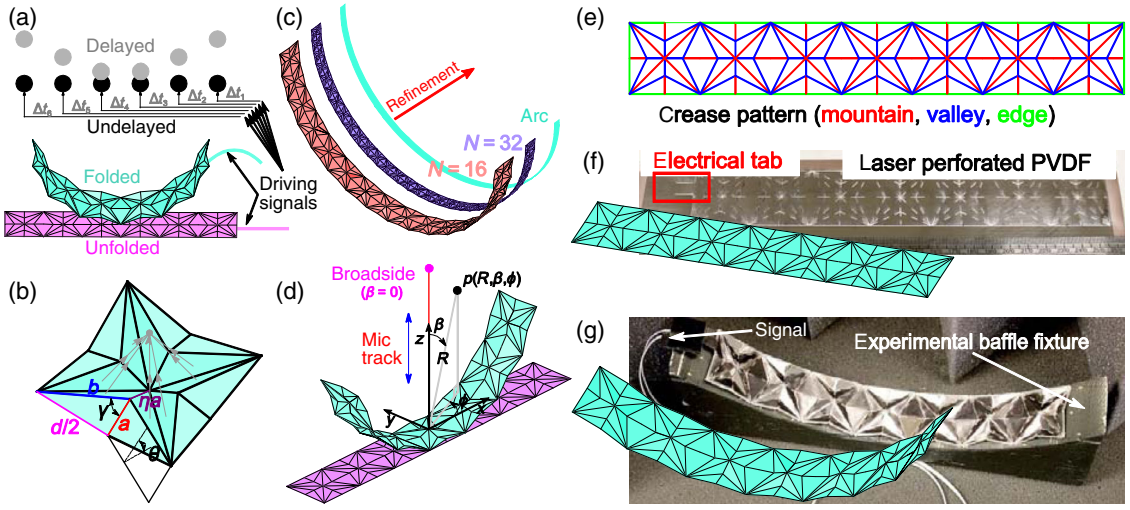

FIG. 1. Overview of the concept and experimental undertakings. (a) Virtual repositioning due to time delay and actual repositioning due to folding. (b) Geometric notation of the star constituent, and the gray dot refers to acoustic energy focusing. (c) Approximation of the arc radiator by refining the foldable tessellated array. (d) Schematic of measuring the broadside acoustic pressure as a function of axial distance R. (e) Crease pattern of foldable tessellations for concave curvature. (f) Piezoelectric PVDF film perforated by a laser cutter. (g) Foldable tessellated array proof-of-concept specimen ($N = 7$) made of substrate and PVDF.

properties, including phononics, photonics, radio-frequency communications, and more. Moreover, we quantitatively assess the similarities of tessellated arrays and classical, ideal radiators. This knowledge elucidates the connections between ideal wave radiators and receivers and the foldable, tessellated arrays that aim to approximate the ideal. By the broad roots of wave physics and wide-reaching relevance of geometry in governing wave properties, this concept may inspire investigations throughout the disciplines of acoustics, optics, and electromagnetics. Therefore, through the example of origami-inspired, reconfigurable acoustic arrays, this research propels fundamental and applied knowledge relevant to multiple physical domains that may favorably leverage origami folding principles to steer and guide waves with simple effectiveness and straightforward adaptability.

Here, we examine acoustic arrays realized by a linear assembly of transducer elements formed from star-shaped constituents [Figs. 1(b) and 1(c)]. The crease pattern is presented in Fig. 1(e). The geometric shape of the constituent is ruled by edge length d, length ratio η, and folding angle θ. By the inward-curving conformation obtained by folding, the assembled array is suggestive of a means to focus energy at a point near the radius of curvature. Indeed, concave arcs are ideal one-dimensional acoustic radiators [27]. Intuitively, the refinement of the tessellated array approximates the arc geometry [Fig. 1(c)].The curvature generated by the tessellated array represents a broader range of the reconfigurable tessellated platforms.

II. CHARACTERIZATION OF ACOUSTIC ENERGY FOCUSING IN THE NEAR FIELD

To facilitate the understanding of the characteristics of the foldable, tessellated array, a theoretical approach to predict the radiated acoustic field is established. The reconfigured geometry of tessellated facets according to kinematic folding is derived. With the information of the spatial distribution of the facet, we use Rayleigh's integral [28,29] to quantify the acoustic pressure in the acoustic fluid resulting from oscillating facets, which bridges the wave-energy delivery and the adaptable shape of the origami-inspired array. The complete derivations are provided in Sec. 2 of Ref. [30]. The boundary element method (BEM) is utilized for the numerical verification of the analytical framework [31], while the proof-of-concept specimen shown in Figs. 1(f) and 1(g) is used for experimental validation.

To test the veracity of the analytical framework, Fig. 2 characterizes the broadside $\beta = 0°$, near-field acoustic-pressure amplitude in air as a function of axial distance R normalized by wavelength λ. Here, near field refers to the acoustic region from the source surface to the transition distance $R_{TR} = D^2/4\lambda$, where D is the array length [32]. The axial distance R is shown in Fig. 1(d) respecting an array that possesses seven constituents. Analytical, numerical, and experimental results for 10 kHz excitation are given in Figs. 2(a), 2(b), and 2(c) for folding angles $\theta = 0°$, 10°, and 20°, respectively. For the unfolded case in Fig. 2(a), the acoustic-pressure amplitude primarily reduces for an increasing distance from the array, an intuitive result because wave energy reduces when radiating away from a source [28]. When the tessellated array is folded to 10° to adopt the concave curvature shown in Fig. 2(b), it is observed that the acoustic pressure fluctuates and a maximum occurs at $R \approx 3.94\lambda$. Thus, the folding-induced repositioning of tessellated elements from $\theta = 0°$ to 10° tailors the wave energy from dispersed to focused. For $\theta = 10°$, the radius of the curvature of the array is 4.05λ. In other words, the origami

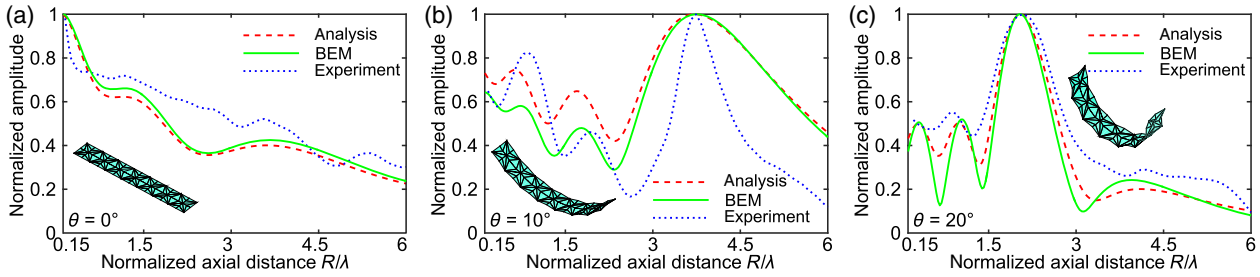

FIG. 2. Theory verification and validation. Normalized amplitude of the broadside acoustic pressure of a foldable tessellated array ($N = 7$) as a function of normalized axial distance R/λ. Analysis (dashed red curve), BEM (solid green curve), and experimental (dotted blue curve) results. Folding angles θ are (a) 0°, (b) 10°, and (c) 20°, respectively. The driving frequency is 10 kHz, array length $D = 7.2\lambda$, and transition distance $R_{TR} = 12.96\lambda$.

geometry approximates the ideal acoustical geometry by the comparable focal lengths. For the folding angle $\theta = 20°$ in Fig. 2(c), the focal point is shifted to 1.90λ with decreased geometric focal length 2.01λ. Such an adaptation of acoustic wave energy empowered by the topological reconfiguration of transducer elements exemplifies the potential of the concept explored here. Although the breadth of the measured peak in Fig. 2(b) is narrower than the analytical and numerical predictions, potentially due to small imperfections in the proof-of-concept specimen such as the separation of the polyvinylidene fluoride (PVDF) film with the substrate during folding, the overall agreement in Fig. 2 establishes the veracity of the analytical framework. Further verifications and validations are given in Ref. [30].

III. CONTRAST BETWEEN TESSELLATED AND PHASED ARRAYS

We then leverage the analytical framework to quantify the distinctions between digital control techniques and foldable tessellated arrays. The contrast is made for acoustic waves delivered to the near or far field, which are relevant demands for many wave-guiding applications [19,33,34]. While the phased array uses time delays to guide the wave energy to a near-field focal point at the axial distance $R = F$ [see Supplemental Material Eq. (25) [30]], the tessellated array is folded so that the radius of curvature of the array is $r = F$. The unfolded tessellated array and phased array are prescribed the same length for the sake of a direct contrast. In Figs. 3(a)–3(c), the left half of the subfigure presents the acoustic pressure for the phased array, while the predictions for the tessellated array are shown in the right. In the unshaded middle of each subfigure is a black dot that indicates the ideal focal point $F = 32\lambda$. The driving frequency is 1 MHz, because acoustic wave focusing is more often relevant in ultrasonic applications [19,33,35]. The array length D is 16λ, while the number of elements N is increased from $N = 4$ in Fig. 3(a), to $N = 8$ in Fig. 3(b), and finally to $N = 32$ in Fig. 3(c). Results in Figs. 3(a)–3(c) are normalized by the maximum acoustic-pressure amplitude for $N = 32$.

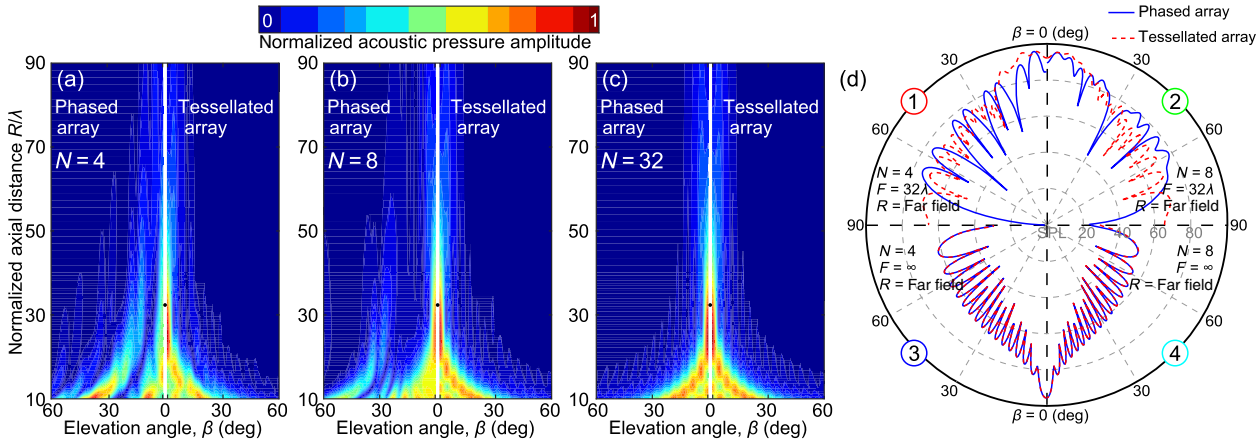

FIG. 3. Comparison between virtual and actual repositioning of array elements. (a)–(c) Near-field acoustic pressure as a function of elevation angle β and normalized axial distance R/λ. Each plot contrasts the phased array (left) with the tessellated array (right). The black dot in the middle denotes the target focal point. The number of elements N is (a) 4, (b) 8, and (c) 32. (d) Far-field sound pressure level (SPL) as a function of elevation angle β at $R = 300\lambda$. Each quadrant contrasts the phased array (solid blue curve) with the tessellated array (dashed red curve). For all plots, the driving frequency is 1 MHz, array length $D = 16\lambda$, and transition distance $R_{TR} = 64\lambda$.

The results in Fig. 3 reveal that a digitally controlled array is less adept at guiding wave energy using the same number of elements than a foldable tessellated array. When the arrays include $N = 4$ elements, Fig. 3(a) shows that a large proportion of radiated energy from the phased array spills out of the focal axis and into adjacent angular regions. Comparatively, the tessellated array achieves a reasonably strong focus close to the ideal focal point (black dot) without such a large diffusion. Quantifying the differences, the greatest normalized pressure amplitude of a sidelobe at the focal point is 0.35 for the phased array, while it is only 0.11 for the tessellated array. In terms of focusing, the tessellated array delivers a pressure amplitude of 0.88 to the focal point, while the phased array achieves 0.52. The stronger sidelobes of the phased array are also observed in the far field [Fig. 3(d), quadrant 1] when compared to the diffused radiation by the tessellated array. This is reflected by the depth of the nodes: The deepest node for the phased array is around 35 dB, while the greatest node depth is less than 20 dB for the tessellated array. For focused array applications, the energy concentration is desired only at the focal point, so that a diffuse far field has advantages [36]. Figure 3(d), quadrant 3, shows that a nearly identical angular distribution is achieved when the phased and tessellated arrays are unfocused, $F = \infty$, thus confirming their equivalence in the limiting case.

With the increase of elements in the arrays to $N = 8$, the near-field energy spillover by the phased array is reduced but not eliminated [Fig. 3(b)], while the tessellated array yields more intense wave focusing around $F = 32\lambda$. Thus, a greater number of elements enables the phased array to more closely approximate the wave guiding of the tessellated array. The corresponding far-field contrasts in Fig. 3(d), quadrants 2 and 4, show a similar convergent behavior. Finally, for $N = 32$, Fig. 3(c) shows that the arrays are nearly equivalent. Consequently, for methods of digital beam forming to achieve ideal wave focusing, a sufficiently great number of transducer elements must be controlled to approximate the arc that delivers energy to the focal point. This contrasts with a continuous distribution of elements over the tessellated folding pattern that approximates an arc geometry. This finding reveals that the wave-guiding capabilities of tessellated arrays are less sensitive to the number of transducer elements than phased arrays. From another perspective, the number of independent signal channels is N for the phased array, while the tessellated array uses one channel to uniformly drive all tessellated facets; see Fig. 1(a). Because N is often >100 in beam-forming applications [19,35], this suggests that reconfigurable tessellated arrays may be simpler and more cost effective to deploy than digital methods.

IV. COMPARISON OF TESSELLATED ARRAY TO THE CLASSICAL GEOMETRIC RADIATOR

As shown in Fig. 1(c), the refinement of the tessellated array to include a greater number of constituents approximates an arc of the same radius of curvature. Therefore, we hypothesize that a close tie may exist between the acoustic wave propagation from foldable tessellated arrays and ideal, geometric acoustical radiators. Indeed, the roots that ground both concepts of wave radiators are interconnected and explicitly characterized through our results shown in Fig. 4 (see also Supplemental Material, Sec. 5 [30]).

In Figs. 4(a)–4(c), the horizontal axes are normalized axial distance R/λ, while the vertical axes are normalized array or arc curvatures, governed by either folding in

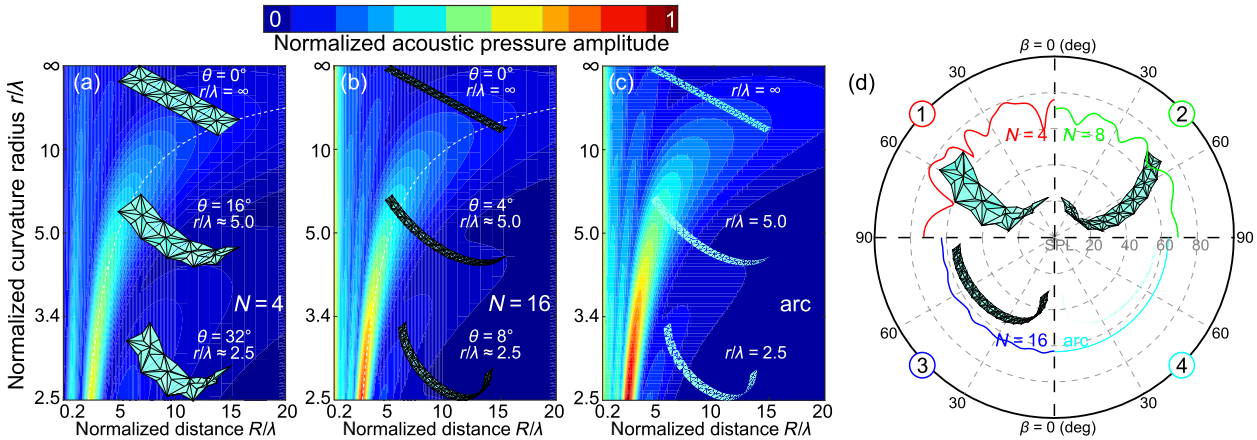

FIG. 4. Comparison of the tessellated array to ideal geometrical acoustics. (a)–(c) Near-field acoustic pressure at broadside as a function of normalized axial distance R/λ and normalized curvature radius r/λ. The acoustic radiators are a tessellated array (a) $N = 4$, (b) $N = 16$, and (c) arc radiator, respectively. The dashed white line is the geometric focal length of the curved array. The driving frequency is 1 MHz, and the length of an unfolded array or arc is $D = 8\lambda$. (d) Far-field SPL as a function of elevation angle β at $R = 300\lambda$. Each plot compares the tessellated arrays of different refinements (1st quadrant $N = 4$, 2nd quadrant $N = 8$, and 3rd quadrant $N = 16$) with the arc radiator (4th quadrant). The driving frequency is 20 kHz, length of an unfolded array or arc $D = 16\lambda$, and transition distance $R_{TR} = 64\lambda$.

Figs. 4(a) and 4(b) or the arc radius in Fig. 4(c). The arc length is the same as the unfolded array length, while pressure amplitudes in Figs. 4(a)–4(c) are normalized by the maximum in Fig. 4(c). Compared to the acoustic energy focusing delivered by the arc in Fig. 4(c), the tessellated array requires sufficient refinement to approximate the focused acoustic energy. The array of $N = 4$ constituents [Fig. 4(a)] achieves about 50% of the peak pressure, whereas the array with $N = 16$ constituents [Fig. 4(b)] delivers 89% of the peak pressure that the arc provides to $r/\lambda = 2.5$. The enhanced focusing at radial locations with smaller normalized curvatures r/λ is associated with an increasing wave convergence. Yet, even for further focal distances, tessellated arrays provide considerable focusing near in magnitude to the ideal arc. For instance, for $r/\lambda = 6.0$, the tessellated arrays with $N = 4$ and 16 elements achieve normalized pressures of 0.40 and 0.45, respectively, which is comparable to the normalized pressure 0.49 achieved by the arc. Being a slice of a baffled, hemispherical monopole, the ideal arc delivers omnidirectional wave radiation to the far field [37]. Likewise, the far-field wave radiation of the tessellated array also converges to this trend for sufficiently large N. Indeed, for the tessellated array of $N = 16$ [Fig. 4(d) quadrant 3], the SPL ripple is only 2 dB over the whole elevation angle range, emphasizing the close approximation of the far-field response of the ideal arc geometry.

V. CONCLUSIONS

These findings reveal that a hierarchy of wave-guiding approaches may be delineated. On one side are ideal radiators and receivers like the arc. While unmatched acoustic characteristics are achieved by such geometric radiators, the need for real-time adaptation may pose challenges to reconfigure the geometry. On the other side are digital methods that may suffer from spatial aliasing that have motivated researchers to compose robust beamforming methods [38]. Spanning the ideal and digital methods of wave guiding are foldable tessellated arrays. Using origami-inspired folding patterns with a low-dimensional shape reconfiguration, we find that the near- and far-field wave radiation characteristics are adaptable in real time and may coarsely approximate ideal wave-guiding capabilities of geometric acoustics. By the attention to a linear array architecture, our findings enable the direct comparison among these wave-guiding approaches and reveal the merits of origami-inspired concepts for acoustic wave guiding. Acoustic reciprocity also dictates that these insights are equally valid for receivers, such as microphone arrays for selective listening. Indeed, portable and deployable wave-guiding devices have numerous applications, such as medical probes [33,35], mobile underwater monitoring [39], and particle manipulators [40]. Moreover, although our studies give attention to acoustic physics, a concept of foldable tessellated arrays with greater effectiveness may be extended to other wave physics, including electromagnetics and optics, where lens and array principles are likewise employed.

ACKNOWLEDGMENTS

The authors acknowledge Dr. Kazuko Fuchi of the University of Dayton Research Institute and Drs. Phil Buskohl, Greg Reich, and James Joo of the Air Force Research Laboratory for helpful conversations. R. L. H. acknowledges funds from the Department of Mechanical and Aerospace Engineering at The Ohio State University. D. T. L. acknowledges support from the Acoustical Society of America via the 2016 Robert W. Young Award for Undergraduate Student Research in Acoustics and from the OSU College of Engineering Honors Research Scholarship.

[1] *Origami 5: Fifth International Meeting of Origami Science, Mathematics, and Education*, edited by P. Wang-Iverson, R. J. Lang, and M. Yim (CRC Press, Boca Raton, FL, 2011).
[2] J. L. Silverberg, A. A. Evans, L. McLeod, R. C. Hayward, T. Hull, C. D. Santangelo, and I. Cohen, Using origami design principles to fold reprogrammable mechanical metamaterials, Science **345**, 647 (2014).
[3] J. T. B. Overvelde, J. C. Weaver, C. Hoberman, and K. Bertoldi, Rational design of reconfigurable prismatic architected materials, Nature (London) **541**, 347 (2017).
[4] H. Yasuda and J. Yang, Reentrant Origami-Based Metamaterials with Negative Poisson's Ratio and Bistability, Phys. Rev. Lett. **114**, 185502 (2015).
[5] L. H. Dudte, E. Vouga, T. Tachi, and L. Mahadevan, Programming curvature using origami tessellations, Nat. Mater. **15**, 583 (2016).
[6] S. Li, H. Fang, and K. Wang, Recoverable and Programmable Collapse from Folding Pressurized Origami Cellular Solids, Phys. Rev. Lett. **117**, 114301 (2016).
[7] A. E. Marras, L. Zhou, H. J. Su, and C. E. Castro, Programmable motion of DNA origami mechanisms, Proc. Natl. Acad. Sci. U.S.A. **112**, 713 (2015).
[8] J. L. Silverberg, J.-H. Na, A. A. Evans, B. Liu, T. C. Hull, C. D. Santangelo, R. J. Lang, R. C. Hayward, and I. Cohen, Origami structures with a critical transition to bistability arising from hidden degrees of freedom, Nat. Mater. **14**, 389 (2015).
[9] S. Waitukaitis, R. Menaut, B. G. G. Chen, and M. van Hecke, Origami Multistability: From Single Vertices to Metasheets, Phys. Rev. Lett. **114**, 055503 (2015).
[10] S. Li and K. W. Wang, Fluidic origami with embedded pressure dependent multi-stability: A plant inspired innovation, J. R. Soc. Interface **12**, 20150639 (2015).
[11] K. Fuchi, A. R. Diaz, E. J. Rothwell, R. O. Ouedraogo, and J. Tang, An origami tunable metamaterial, J. Appl. Phys. **111**, 084905 (2012).
[12] S. Bildik, S. Dieter, C. Fritzsch, W. Menzel, and R. Jakoby, Reconfigurable folded recflectarray antenna based upon

liquid crystal technology, IEEE Trans. Antennas Propag. **63**, 122 (2015).
[13] T. H. Ware, M. E. McConney, J. J. Wie, V. P. Tondiglia, and T. J. White, Voxelated liquid crystal elastomers, Science **347**, 982 (2015).
[14] J. Zhou and S. S. Sheiko, Reversible shape-shifting in polymeric materials, J. Polym. Sci. **54**, 1365 (2016).
[15] S. Babaee, J. T. B. Overvelde, E. R. Chen, V. Tournat, and K. Bertoldi, Reconfigurable origami-inspired acoustic waveguides, Sci. Adv. **2**, e1601019 (2016).
[16] M. Thota, S. Li, and K. W. Wang, Lattice reconfiguration and phononic band-gap adaptation via origami folding, Phys. Rev. B **95**, 064307 (2017).
[17] E. Boatti, N. Vasios, and K. Bertoldi, Origami metamaterials for tunable thermal expansion, Adv. Mater. **29**, 1700360 (2017).
[18] B. D. Van Veen and K. M. Buckley, Beamforming: A versatile approach to spatial filtering, IEEE ASSP Mag. **5**, 4 (1988).
[19] F. A. Jolesz and K. H. Hynynen, *MRI-Guided Focused Ultrasound Surgery* (CRC Press, New York, 2007).
[20] L. Azar, Y. Shi, and S. C. Wooh, Beam focusing behavior of linear phased arrays, NDT&E Int. **33**, 189 (2000).
[21] I. F. Akyildiz, D. Pompili, and T. Melodia, Underwater acoustic sensor networks: Research challenges, Ad Hoc Networks **3**, 257 (2005).
[22] S. A. Zirbel, R. J. Lang, M. W. Thomson, D. A. Sigel, P. E. Walkemeyer, B. P. Trease, S. P. Magleby, and L. L. Howell, Accommodating thickness in origami-based deployable arrays, J. Mech. Des. **135**, 111005 (2013).
[23] T. U. Lee and J. M. Gattas, Geometric design and construction of structurally stabilized accordion shelters, J. Mech. Rob. **8**, 031009 (2016).
[24] R. L. Harne and D. T. Lynd, Origami acoustics: Using principles of folding structural acoustics for simple and large focusing of sound energy, Smart Mater. Struct. **25**, 085031 (2016).
[25] D. T. Lynd and R. L. Harne, Strategies to predict radiated sound fields from foldable, Miura-ori-based transducers for acoustic beamfolding, J. Acoust. Soc. Am. **141**, 480 (2017).
[26] C. Zou and R. L. Harne, Adaptive acoustic energy delivery to near and far fields using foldable, tessellated star transducers, Smart Mater. Struct. **26**, 055021 (2017).
[27] H. O'Neil, Theory of focusing radiators, J. Acoust. Soc. Am. **21**, 516 (1949).
[28] L. E. Kinsler, A. R. Frey, A. B. Coppens, and J. V. Sanders, *Fundamentals of Acoustics* (Wiley, New York, 2000).
[29] E. G. Williams, *Fourier Acoustics: Sound Radiation and Nearfield Acoustical Holography* (Academic, San Diego, 1999).
[30] See Supplemental Material at http://link.aps.org/supplemental/10.1103/PhysRevApplied.9.014009 for theoretical modeling and experimental details and supporting analytical, experimental, and numerical results.
[31] V. C. Henriquez and P. M. Juhl, OpenBEM—An open source Boundary Element Method software in Acoustics, in *Proceedings of Internoise 2010, Lisbon, Portugal* (Publisher, location, 2010), pp. 1–10.
[32] O. T. Von Ramm and S. W. Smith, Beam steering with linear arrays, IEEE Trans. Biomed. Eng. **BME-30**, 438 (1983).
[33] M. Postema, *Fundamentals of Medical Ultrasonics* (Spon Press, New York, 2011).
[34] B. Truax, *Acoustic Communication* (Ablex, Westport, 2001).
[35] B. W. Drinkwater and P. D. Wilcox, Ultrasonic arrays for non-destructive evaluation: A review, NDT&E Int. **39**, 525 (2006).
[36] V. Auboiroux, L. Petrusca, M. Viallon, T. Goget, C. D. Becker, and R. Salomir, Ultrasonography-based 2D motion-compensated HIFU sonication integrated with reference-free MR temperature monitoring: A feasibility study ex vivo, Phys. Med. Biol. **57**, N159 (2012).
[37] H. F. Olson, *Elements of Acoustical Engineering* (Van Nostrand, New York, 1940).
[38] J. Li and P. Stoica, *Robust Adaptive Beamforming* (Wiley, New York, 2005).
[39] C. H. Sherman and J. L. Butler, *Transducers and Arrays for Underwater Sound* (Springer, New York, 2007).
[40] A. Marzo, S. A. Seah, B. W. Drinkwater, D. R. Sahoo, B. Long, and S. Subramanian, Holographic acoustic elements for manipulation of levitated objects, Nat. Commun. **6**, 8661 (2015).

Supplementary Information to
Acoustic wave guiding by reconfigurable, tessellated arrays

Chengzhe Zou, Danielle T. Lynd, and Ryan L. Harne*

Department of Mechanical and Aerospace Engineering, The Ohio State University, Columbus, OH 43210, USA

** Correspondence to: harne.3@osu.edu*

In the following sections, the proof-of-concept specimen fabrication and experimentation are detailed. Then the geometry of the foldable, tessellated array is mathematically defined according to assumptions of rigid foldability. The geometric definition paves the way for the subsequent analytical derivation of acoustic pressure prediction for locations in near and far fields. To assess the accuracy of the theoretical framework in the far field, the analysis is verified and validated by numerical and experimental efforts, respectively, which complements the verification and validation given in the main text. Next, for a comprehensive understanding of the nuanced distinctions between the tessellated array and phased array, analytical comparisons are provided for scenarios of sound radiation to near and far fields. Finally, the influences on the radiated acoustic field by refining the tessellated array is further explored by extensive comparisons with the ideal arc radiator.

1 Experimental setup

1.1 Specimen fabrication

The components of the proof-of-concept experimental specimen are presented in Fig. 1(f). The fabrication process includes four steps: scoring a plastic substrate along the folding pattern shown in Fig. 1(d), perforating piezoelectric PVDF film along the same creases, assembling the substrate and film, and building the electrical connections.

The substrate of the foldable tessellation is made of polypropylene (ePlastics) with thickness 762 μm. The substrate is scored by a laser cutter (Full Spectrum Laser H-20x12). This process discretizes the continuous plastic substrate into planar facets that fold with the scored creases in a hinge-like motion. PVDF film is used to drive the substrate to radiate acoustic waves. The thickness of the film (Measurement Specialties) is 52 μm, and the electrodes that bound the film are copper-nickel. To decrease folding-induced stretching around the hinges, the PVDF is perforated by the laser cutter along the creases, as shown in Fig. 1(e). Then the PVDF film is attached to the substrate by a single strip of double-sided tape while the substrate is in the unfolded configuration. This assembly method helps to ensure the coincidence of scored hinges and perforations. As observed in Fig. 1(e), a small tab of PVDF film extends from the film sheet of the tessellation. This tab is used to make electrical contact to the specimen without influencing the tessellated surface. Two thin-gauge wires are soldered to copper tape that is bonded to both sides of the PVDF film tab. The wires are then used to drive the film with the input signal, which causes the PVDF to expand and contract at the same frequency as the input. By being bonded to the polypropylene substrate, the oscillating film permits the proof-of-concept experimental specimen to radiate acoustic waves.

1.2 Experimental system description

The experiments are undertaken inside a hemi-anechoic chamber with dimensions 7.8 m by 10.9 m by 4.7 m. To maintain the prescribed folded state, the specimen is affixed to custom-made wooden mounts that match the curvature of the tessellated array for a given fold angle. The wooden mount provides an effective acoustic baffle for the specimen, which is desired in acoustic measurements of sound sources [1].

For the near field measurements, a microphone (PCB Piezotronics 130E20) is linearly guided along the broadside angular location to measure the acoustic pressure fluctuation as a function of axial distance, as illustrated in Fig. 1(c). For the far field directivity measurements, the microphone traverses according to a hemispherical arm of radius 2 m. At this radial distance from the specimen, the far field conditions [2] are satisfied for the characteristic dimension of the specimen and driving frequencies considered here. The range of the elevation angle β inscribed by the traverse is [0°, 90°], while the corresponding angular displacement is recorded by a rotary encoder (Signswise).

The harmonic driving signal is created in MATLAB Data Acquisition Toolbox and then sent to the power amplifier (Pyle PFA300). The amplified signal is delivered to an audio output transformer (RadioShack 2731380) and the output voltage directly drives the tessellated transducer array. The sound pressure and angular displacement data are sent to MATLAB for post-processing. The sampling frequency is 131 kHz while the recorded data is digitally filtered with a dynamic fourth-order Butterworth filter covers the upper and lower 3 kHz of the driving frequency.

Data of sound pressure level and acoustic pressure amplitude obtained by these techniques are presented in the main text and this Supplementary Information as functions of radial distance or angular displacement. As such, the measurements are continuous in time and are processed over short time durations to identify the effective instantaneous axial distance, angular displacement, sound pressure level, and/or acoustic pressure amplitude.

2 Theoretical model formulation

2.1 Geometric modeling

As shown in Supplementary Fig. 1(a), the vertices of the same color in the foldable, tessellated array lie along corresponding colored circles that are parallel to the $x-z$ plane. Demonstrating the veracity of this fact is straightforward. Namely, the connection lines between two adjacent vertices of the same color are of the same length by rotational periodicity of the tessellation, so that the connection lines may be viewed as the edges of an inscribed polygon of a circle. Because the tessellated array is linear, the y coordinates of these circle centers are determined by the kinematic shape change of the constituent. The kinematic shape change is previously reported in Ref. [3]. In addition, although there are multiple circles, the projections of all the centers in the $x-z$ plane are coincident [4]. Thus, only x and z coordinates of one circle center are required to fully determine the center location. Hereafter, circle 3 is discussed.

The geometry of the folded constituent lays the foundation to derive the topological reconfiguration of the tessellated array. The constituent geometric and folding parameters are labeled in Fig. 1(a), among which are the edge length d, length ratio η, and folding angle θ. These three variables are the independent features that define the topology of the tessellated constituent. The relations of other parameters become

$$a = \frac{1}{2(\eta+1)} d \tag{1a}$$

$$b = \frac{\sqrt{\eta^2+2\eta+2}}{2(\eta+1)} d \tag{1b}$$

$$\gamma = \tan^{-1}(\eta+1) \tag{1c}$$

The locations of the vertices of constituent are derived from the well-known Miura-ori folding pattern [3], and Eq. (1) defines the parallelogram of corresponding Miura-ori. Along with folding angle θ, the folding extents of the unit cell of Miura-ori (S, L, H, and V) are easily obtained based on Ref. [5], which are then employed to express the coordinates of the vertices of the constituent. It is important to note that S, L, H, and V are each functions of the folding angle θ.

As the vertices of constituent 1 in Supplementary Fig. 1(b), the positions of points 1, 2, 3, and 4 in the given coordinate system respectively are

$$(x_1, y_1, z_1) = \left(-S, S, -(V+\eta L)\sin\kappa - \eta H\cos\kappa\right) \tag{2a}$$

$$(x_2, y_2, z_2) = \left(-(\eta+1)L\cos\kappa + (\eta-1)H\sin\kappa, 0, -(\eta+1)L\sin\kappa - (\eta-1)H\cos\kappa\right) \tag{2b}$$

$$(x_3, y_3, z_3) = \left(-S, -S, -(V+\eta L)\sin\kappa - \eta H\cos\kappa\right) \tag{2c}$$

$$(x_4, y_4, z_4) = \left(S, S, -(V+\eta L)\sin\kappa - \eta H\cos\kappa\right) \tag{2d}$$

where (x_i, y_i, z_i) respectively refers to x, y, and z coordinates of the i^{th} vertice in the coordinate system shown in Supplementary Fig. 1(b). Also, $\kappa = \left|\ln\left[\frac{\sqrt{H^2+(L+V)^2-S^2}-jS}{H-j(L+V)}\right]\right|$ is the rotation angle to transform the Miura-ori coordinate to the star constituent system [3]. It is worth recalling that these nodal locations and rotations are implicitly dependent upon the folding angle θ by their dependence upon S, L, H, and V.

To derive the coordinates of circle 3, the locations of points 1, 4, and 5 are required. The locations for points 1 and 4 are given in Eq. (2). These two constituents are shown in Supplementary Fig. 1(b) to be mirrored about the plane P defined by points 1, 2, and 3. Consequently, point 5 is the reflection of point 4 about this plane.

The expression of plane P using vector algebra is

$$\vec{n}\left(x\vec{i}+y\vec{j}+z\vec{k}\right)=C \tag{3}$$

where the normal vector $\vec{n}=\vec{v}_{12}\times\vec{v}_{23}$ and the constant $C=\vec{n}\vec{v}_1$.

The projection of point 4 on plane P can be expressed as

$$\vec{v}_{4\_proj}=\vec{v}_4+\vec{v}_{44\_proj}=\vec{v}_4+g\vec{n} \tag{4}$$

where g is a temporary coefficient.

Substituting Eq. (4) into Eq. (3) yields

$$g=\frac{C-\vec{n}\vec{v}_4}{\left|\vec{n}\right|^2} \tag{5}$$

Then the position vector of point 5 is

$$\vec{v}_5=\vec{v}_4+2\frac{C-\vec{n}\vec{v}_4}{\left|\vec{n}\right|^2}\vec{n} \tag{6}$$

As shown in Supplementary Fig. 1(b), L_1 and L_2 are the perpendicular bisectors of chords L_{14} and L_{15}, respectively. In the $x-z$ plane that circle 3 exists, the slopes of L_{14} and L_{15} are respectively

$$\nabla L_{14}=\frac{z_4-z_1}{x_4-x_1} \tag{7a}$$

$$\nabla L_{15}=\frac{z_5-z_1}{x_5-x_1} \tag{7b}$$

where ∇ refers to the slope of the line in the $x-z$ plane.

Since $L_1\perp L_{14}$ and $L_2\perp L_{15}$, the slopes of L_1 and L_2 are respectively

$$\nabla L_1=-\frac{x_4-x_1}{z_4-z_1} \tag{8a}$$

$$\nabla L_2=-\frac{x_5-x_1}{z_5-z_1} \tag{8b}$$

The midpoints of L_{14} and L_{15} lie on L_1 and L_2 respectively, yielding

$$z-\frac{z_1+z_4}{2}=-\frac{x_4-x_1}{z_4-z_1}\left(x-\frac{x_1+x_4}{2}\right) \tag{9a}$$

$$z-\frac{z_1+z_5}{2}=-\frac{x_5-x_1}{z_5-z_1}\left(x-\frac{x_1+x_5}{2}\right) \tag{9b}$$

C_3 is the intersection of L_1 and L_2, so the solutions of Eq. (9) are its x and z coordinates

$$x_C=\frac{x_5^2(z_1-z_4)+\left[x_1^2+(z_1-z_4)(z_1-z_5)\right](z_4-z_5)+x_4^2(z_5-z_1)}{2\left[x_1(z_4-z_5)+x_4(z_5-z_1)+x_5(z_1-z_4)\right]} \tag{10a}$$

$$z_C=\frac{x_1\left(x_4^2-x_5^2+z_4^2-z_5^2\right)+x_4\left(x_5^2-x_1^2-z_1^2+z_5^2\right)+x_5\left(x_1^2-x_4^2+z_1^2-z_4^2\right)}{2\left[x_1(z_4-z_5)+x_4(z_5-z_1)+x_5(z_1-z_4)\right]} \tag{10b}$$

The radii of the four circles in Supplementary Fig. 1(a) respectively are

$$r_1=\sqrt{(x_6-x_C)^2+(z_6-z_C)^2} \tag{11a}$$

$$r_2=\sqrt{(x_2-x_C)^2+(z_2-z_C)^2} \tag{11b}$$

$$r_3=r_4=\sqrt{(x_1-x_C)^2+(z_1-z_C)^2} \tag{11c}$$

These radii are governed by the folding angle θ alone once the geometry size is determined, and consequently there is only one independent radius among them to reflect the folding-induced curvature. In this work, r_1 is defined as the radius of the curvature r.

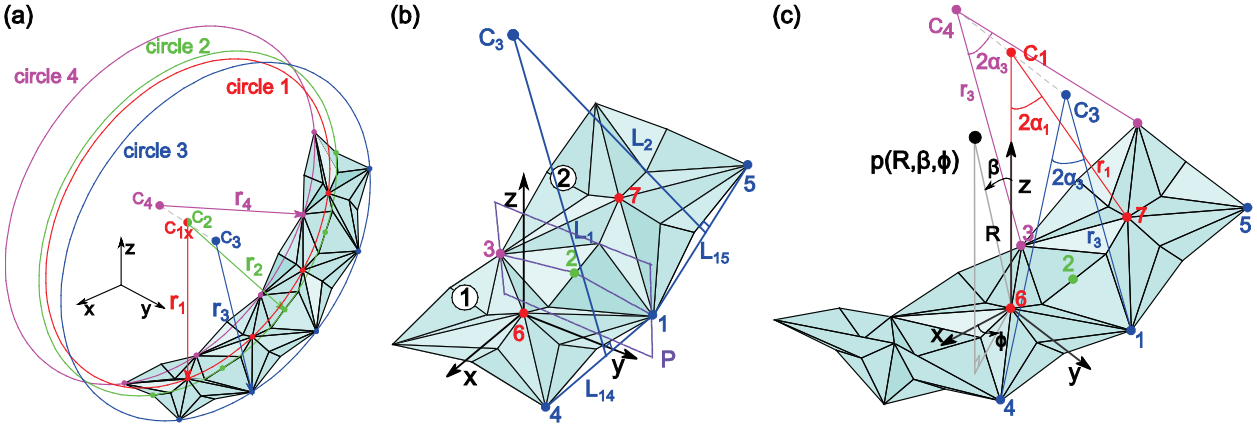

Supplementary Figure 1. (a) The schematic representing the curvatures of tessellated array in which the vertices of different colors lie on the circumferences of corresponding colored circles. C and r refer to circle center and radius, respectively. (b) Tessellated array ($N=2$) used to derive the radii of curvatures. (c) The analytical model notation to predict the sound pressure radiated from the transducer array to the far field point $p(R,\beta,\phi)$.

2.2 Far field directivity prediction

For the field point $p(R,\beta,\phi)$ in Supplementary Fig. 1(c), the beam pattern of the transducer array is a function only of elevation angle β and azimuth angle ϕ when the distance R from the effective source

center to the field point meets the far field conditions [1]. In acoustics, it is a convention to quantify the beam pattern by the metric sound pressure level (SPL), which is computed from the acoustic pressure $p(R,\beta,\phi)$ with respect to a reference pressure. By the usage here, the SPL is in decibels dB

$$\mathrm{SPL} = 20\log_{10}\left[\frac{p_{\mathrm{rms}}(R,\beta,\phi)}{p_{\mathrm{ref}}}\right] \tag{12}$$

where the subscript rms is the root mean square value of $p(R,\beta,\phi)$, and $p_{\mathrm{ref}} = 20\,\mu\mathrm{Pa}$.

In Ref. [3], the directivity of the constituent $b(\beta,\phi)$ is derived. Conventionally, the product theorem would conclude that the transducer array beam pattern $B(\beta,\phi)$ is computed as the product of the constituent beam pattern $b(\beta,\phi)$ and the array factor $D(\beta,\phi)$ [1]

$$B(\beta,\phi) = b(\beta,\phi)D(\beta,\phi) \tag{13}$$

The product theorem holds when the transducers are geometrically arranged so that phase differences of waves arriving to the field point from individual transducers are decomposed into a component common to all transducers and a component that is a function of the spatial distribution of arrayed transducers [6]. For arrays composed of lines or planar grids of transducers, the decomposition is possible.

Yet for the folded tessellated array, the elevation angle β and azimuth angle ϕ of individual transducers are different for the same field point which prevents such decoupling. In order to overcome this challenge, here the elevation angle β and azimuth angle ϕ are derived individually for each transducer.

Using vector notations to express the location of the far field point $p(R,\beta,\phi)$

$$\vec{v}_p = x_p\vec{i} + y_p\vec{j} + z_p\vec{k} \tag{14}$$

where $x_p = R\sin\beta\cos\phi$, $y_p = R\sin\beta\sin\phi$, and $z_p = R\cos\beta$.

In the following derivation, the number of transducer elements in the array N is assumed as odd for the sake of simplicity, although this can be easily extended for cases when N is an even number.

Point 6 is the origin of the coordinate system defined in Supplementary Fig. 1(c), and its relation to point 7 is analogous to that between points 4 and 5, therefore the location of point 7 is

$$\vec{v}_7 = \vec{v}_6 + 2\frac{C - \vec{n}\vec{v}_6}{|\vec{n}|^2}\vec{n} \tag{15}$$

The angular periodicity of point 6 is

$$2\alpha_1 = 2\sin^{-1}\left(\frac{l_{67}}{2r_1}\right) \tag{16}$$

where l_{67} is the length of the chord connected by points 6 and 7.

Similarly the angular periodicity of points 1, 3, and 4 is $2\alpha_3 = 2\sin^{-1}\left(\frac{l_{14}}{2r_3}\right)$ (17)

where l_{14} is the length of the chord connected by points 1 and 4.

Therefore the x and z relative positions of points 1, 3, 4, and 6 in i^{th} transducer to center are

$$x_{1C}(i) = x_{3C}(i) = r_3 \sin\left[(2i+1)\alpha_3\right] \tag{18a}$$

$$z_{1C}(i) = z_{3C}(i) = r_3 \cos\left[(2i+1)\alpha_3\right] \tag{18b}$$

$$x_{4C}(i) = r_3 \sin\left[(2i-1)\alpha_3\right] \tag{18c}$$

$$z_{4C}(i) = r_3 \cos\left[(2i-1)\alpha_3\right] \tag{18d}$$

$$x_{6C}(i) = r_1 \sin(2i\alpha_1) \tag{18e}$$

$$z_{6C}(i) = r_1 \cos(2i\alpha_1) \tag{18f}$$

where i is an integer, and $i \in \left[-\frac{N-1}{2}, \frac{N-1}{2}\right]$.

The y coordinates are known from the constituent geometry, so that all the three-dimensional locations of the points 1, 3, 4, and 6 are obtained.

The normal vector of the i^{th} transducer is

$$\vec{n}(i) = \vec{v}_{1(i)3(i)} \times \vec{v}_{1(i)4(i)} \tag{19}$$

The included angle between $\vec{n}(i)$ and $\vec{v}_{6(i)p}$ is the i^{th} elevation angle

$$\beta(i) = \cos^{-1}\left(\frac{\vec{v}_{6(i)p}\vec{n}(i)}{\left|\vec{v}_{6(i)p}\right|\left|\vec{n}(i)\right|}\right) \tag{20}$$

The projection of $\vec{v}_{6(i)p}$ on the i^{th} transducer plane is

$$\vec{v}_{6(i)p\_proj} = \vec{v}_{6(i)p} - \frac{\vec{v}_{6(i)p}\vec{n}(i)}{\left|\vec{n}(i)\right|^2}\vec{n}(i) \tag{21}$$

Then the included angle between $\vec{v}_{6(i)p\_proj}$ and $\vec{v}_{1(i)4(i)}$ is the i^{th} azimuth angle

$$\phi(i) = \cos^{-1}\left(\frac{\vec{v}_{6(i)p\_proj} \vec{v}_{1(i)4(i)}}{\left|\vec{v}_{6(i)p\_proj}\right| \left|\vec{v}_{1(i)4(i)}\right|} \right) \tag{22}$$

Substitute Eqs. (20) and (22) into $b(\beta, \phi)$, and the summation yields the array directivity

$$B(\beta, \phi) = \sum_{i=1}^{N} b(\beta_i, \phi_i) \tag{23}$$

2.3 Near field acoustic pressure prediction

In Section 2.2, the acoustic modeling is derived under far field assumptions, in which spherical acoustic waves emanating from the transducer surface are approximately plane waves when arriving to the far field point [1]. Yet in the near field, the wave fronts from different regions of the array are still mostly spherical at common field points, so that far field approximations do not immediately hold. To predict the sound energy propagated from the tessellated transducer array into near field regions, this research takes advantage of the approach proposed in Ref. [7]. By the approach, a vibrating rectangular panel is discretized into rectangular source elements whose characteristic dimensions are sufficiently small so as to then meet far field criteria [2]. Then, acoustic wave radiation is computed from Rayleigh's integral solved for each sub-area, while the summation of all sub-area contributions yields a full response. With the refinement of the discretization, the phase difference between adjacent sources can be distinguished more accurately, and consequently the prediction gradually converges to the actual acoustic near field.

In this exploration, the tessellated array is discretized into triangular elements. The superposed near field sound pressure is therefore

$$p(R, \beta, \phi, t) = j \frac{\rho_0 \omega u_0}{2\pi} e^{j\omega t} \sum_{i=1}^{M} \left\{ \int_{A_i} \frac{e^{-jkR_i}}{R_i} dA_i \right\} \tag{24}$$

where ρ_0 is the density of the medium; ω is the angular frequency of harmonic excitation; A_i is the area of i^{th} sub-facet; u_0 is the amplitude of the normal velocity over A_i; $k = \omega / c_0$ is the acoustic wavenumber with the sound speed c_0; R_i is the distance from the field point to the center of the i^{th} sub-area; M is the number of the discretized sub-facets. In this work, the fluid media is considered to be air in all computations of acoustic pressure. As such, ρ_0 = 1.104 kg/m^3 and c_0 = 343 m/s.

3 Numerical verification and experimental validation

In this section, the accuracy of the analytical framework is tested against the results of numerical simulations and experiments. Since the near field is investigated in Fig. 2 in the main text, the far field directivity is assessed here.

3.1 Comparison of analytical and numerical results in far field directivity

The boundary element method (BEM) is efficient to numerically solve problems of acoustic radiation and reception since only the boundaries need to be meshed, instead of the whole acoustic medium. To obtain accurate results from BEM, at least six linear elements are used per wavelength to construct the surface mesh. For results presented in Fig. 2 and Supplementary Fig. 2, this guideline is satisfied. The amplitude of the surface normal velocity u_0 is 10 mm/s for all the results of analysis and BEM in the main text and Supplementary Information. The comparison between analytical and numerical results of far field sound pressure level (SPL) for the tessellated array with six constituents, $N = 6$, is presented in Supplementary Fig. 2. The edge length d and length ratio η of the unfolded constituent are 0.02 m and 1, respectively. For ease of visualization, the analytical and BEM results are presented in a mirrored way about the azimuthal location $\phi = 0°$. The top row of Supplementary Fig. 2 provides results considering the tessellated array to be driven at 10 kHz, while the bottom row provides results considering 20 kHz driving. For the columns from left to right, the folding angles θ are 0°, 10°, and 20°, respectively.

Here, locations where the magnitude of SPL is reduced substantially are termed nodes. For the unfolded array $\theta = 0°$ when driven at 10 kHz, Supplementary Fig. 2(a), it is seen that there are 3 nodes at $\phi = 0°$ and no nodes at $\phi = 90°$. This outcome is caused by the distribution of six transducers in a line along the axis with azimuth $\phi = 0°$ so that all six transducers in the array contribute waves with different phase to the far field point. In contrast, for the far field point at $\phi = 90°$, the transducer elements are approximately in parallel, so that no interference occurs among transducer elements. Similar distinctions are seen for the unfolded array $\theta = 0°$ when driven at 10 kHz as shown in Supplementary Fig. 2(d) for 20 kHz. For the broadside location $\beta = 0°$, the angular width of the major lobe for azimuth $\phi = 0°$ is narrower for the tessellated array driven at 20 kHz than at 10 kHz. This is not surprising due to the greater number of acoustic wavelengths that fit between the span from one tessellated transducer constituent to the next at 20 kHz. For both frequencies under $\theta = 0°$, good quantitative agreements between analysis and BEM are observed in Supplementary Fig. 2(a) and (d), which verifies the accuracy of the analysis under the limiting case of the unfolded tessellated array.

The influence of folding is examined by viewing the top row of Supplementary Fig. 2 from left to right. For the folding angle $\theta = 10°$ and driving frequency 10 kHz in Supplementary Fig. 2(b), the wave radiation loses the significance of directive response obtained in the unfolded configuration. Considering $\phi = 0°$ for instance, the depths of the nodes are decreased at both 10 and 20 kHz, when compared to the unfolded results $\theta = 0°$, though slight SPL reductions still exist due to the folding to $\theta = 10°$. When the folding angle is further increased to 20°, the directivity at $\phi = 0°$ is mostly lost so that the array is close to an omnidirectional radiator. This characteristic is favorable for conformal antenna arrays that may require omnidirectional beam patterns in certain applications [6]. In addition, as seen according to the increased folding angle in Supplementary Fig. 2, the broadside SPL is reduced due to the loss of ideal constructive interference that occurs for flat, planar radiators emitting to the broadside location [6].

For the folded states, the agreement between analytical and BEM results is qualitatively good while quantitative discrepancies occur. The BEM method accounts for reflections among facets, which does not contribute to evaluations of Rayleigh's integral that is so commonly used in the assessment of far field wave propagation [1] [8]. On the other hand, the significance of such reflections is minor in absolute pressure difference, since the logarithmic dB scale used for SPL evaluation in Supplementary Fig. 2 may cloud the considerable quantitative agreement achieved between analysis and BEM simulation. In addition, the deviations of the analytical predictions to the BEM results should be considered with respect to the computational requirements of both approaches. The time used to compute the analytical portion of any given sub-figure in Supplementary Fig.2 is around 2.6 s, while the corresponding time required for BEM simulation is around 6.5 hours. Consequently, the analysis is almost four orders of magnitude more time-efficient to deploy than the BEM.

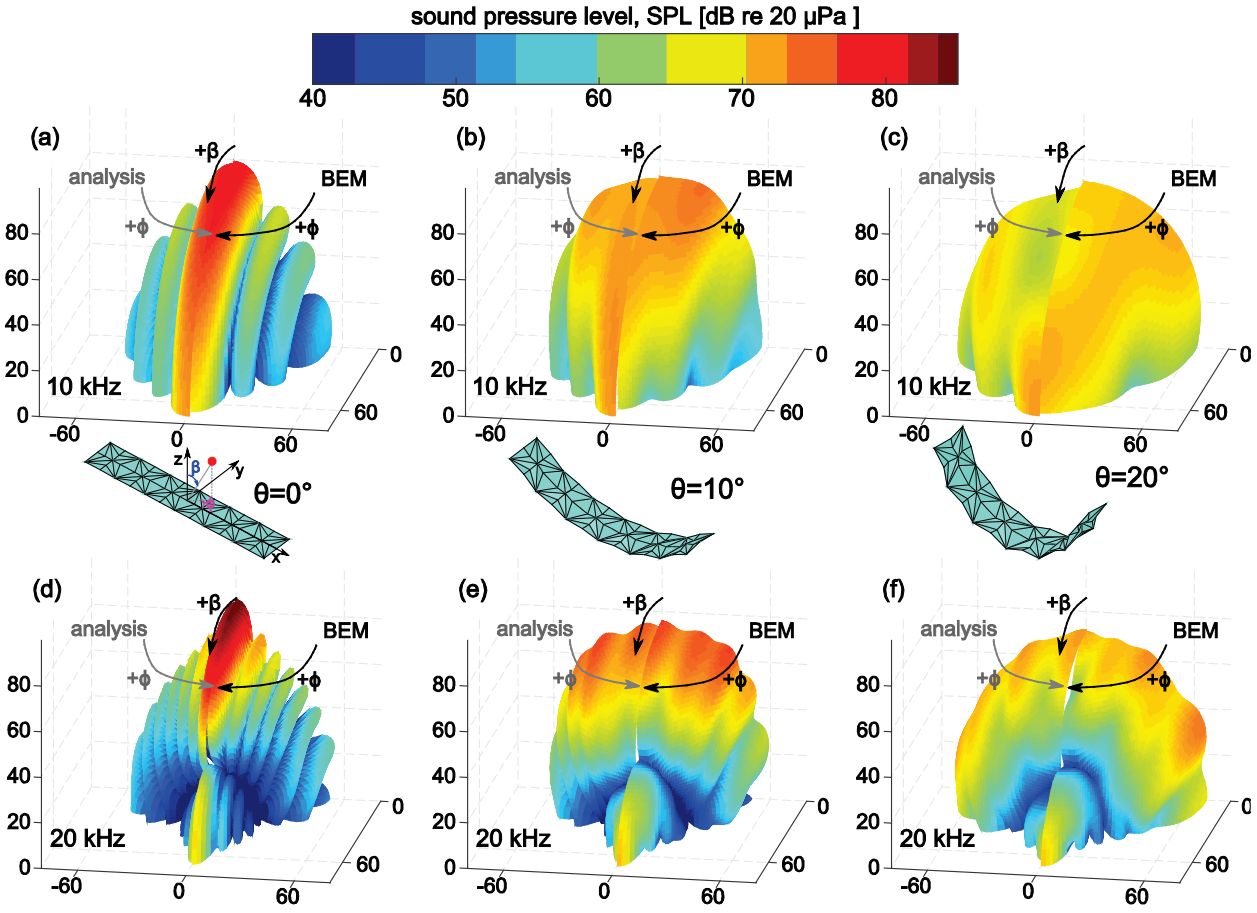

Supplementary Figure 2. Far field sound pressure level (SPL) of tessellated array ($N = 6$) as a function of the elevation angle β and azimuth angle ϕ of the field point. Each plot includes the analysis (left) and BEM (right) results. The spans in x, y, and z axes pertain to SPL and the radial distance from the origin indicates the magnitude of the SPL. Driving frequencies are 10 kHz (top row) and 20 kHz (bottom row). Folding angle (a, d) $\theta = 0°$, (b, e) $\theta = 10°$, and (c, f) $\theta = 20°$.

3.2 Comparison of analytical and experimental results in far field directivity

Experimental validation of the far field analytical predictions is also undertaken. The far field SPL measurements radiated from the proof-of-concept tessellated array specimen are compared with the analytical predictions in Supplementary Fig. 3. The three plots (a, b, c) present the comparison for folding angle $\theta = 0°$, 10°, and 20° from (a) to (b) to (c), respectively. In each sub-figure, results for 9 and 16 kHz driving frequencies are respectively presented using solid and dashed curves. The analytical results are shown in the left-most quadrants, while the measurements are shown in the right-most quadrants.

Considering 9 kHz in Supplementary Fig. 3(a), there are multiple deep nodes in the analytical prediction, and the SPL is decreased by about 30 dB when the field point is moved from broadside to endfire (i.e. from $\beta = 0°$ to $\beta = 90°$) . Both phenomena are observed in the measurements, although the measured nodes are not as deep as those predicted analytically. This is because the ideal constructive interference phenomena characterized by the analysis are rarely achieved in practice due to the influential roles of imperfections on the phase of radiated or received waves in arrays [1]. Despite this practical challenge, for 16 kHz radiation from the tessellated array, the SPL is more directive with greater number of nodes along with more substantial SPL reduction at the endfire condition $\beta = 90°$. These trends are observed in both analytical and experimental results.

As shown in Supplementary Fig. 3(b) for folding angle $\theta = 10°$, the overall sound pressure delivery from the tessellated array to the far field measurement point is much less directive than the unfolded state $\theta = 0°$. For 9 kHz radiation, the nodes are decreased in depth as well as number, while the broadside SPL reduces to 80 dB from 90 dB. Moreover, the SPL difference between broadside $\beta = 0°$ and endfire $\beta = 90°$ cases is lessened to approximately 10 dB. These influences of increased folding of the tessellated array that are measured in the hemi-anechoic chamber are likewise captured well in the analytical predictions in Supplementary Fig. 3(b). When the tessellated array is folded further to $\theta = 20°$, the results of Supplementary Fig. 3(c) conclusively show that the array emits acoustic waves in an omnidirectional way. These findings from the analysis and experiments in Supplementary Fig. 3 are in good agreement to the trends observed by the BEM simulations in Supplementary Fig. 2.

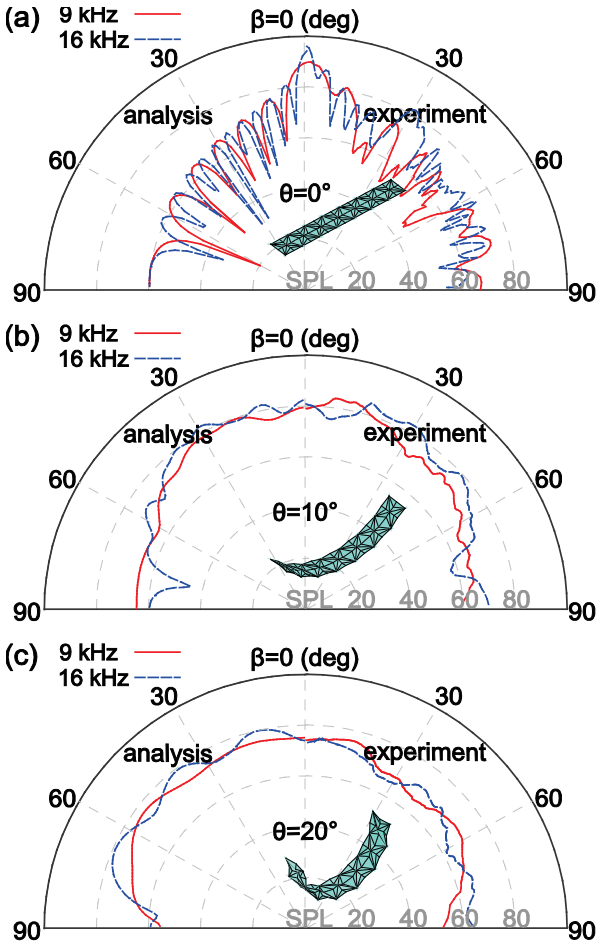

Supplementary Figure 3. Far field sound pressure level (SPL) of tessellated array (N = 7) as a function of the elevation angle β of the field point at azimuth angle ϕ = 0°. Each plot includes the analysis (left) and experiment (right) results. The driving frequencies are 9 kHz (solid red) and 16 kHz (dashed blue). Folding angle (a) θ = 0°, (b) θ =10°, and (c) θ =20°.

4 Contrast between tessellated array and phased array

4.1 Focusing formula of linear phased array

The introduction of time delays to the transducer elements enables phased linear arrays to focus acoustic waves to a specific point. The time delay t_i required for the i^{th} transducer element to focus acoustic energy at broadside is computed from [9]

$$\frac{c_0 t_i}{F} = \left[1+\left(N'\frac{e}{F}\right)^2\right]^{1/2} - \left[1+\left((i-N')\frac{e}{F}\right)^2\right]^{1/2};\ N' = \frac{N-1}{2};\ i = [0, N-1] \tag{25}$$

where N is the number of elements in the linear array, F is the focal length from the array center, and e is the center-to-center spacing between adjacent elements. Eq. (25) is applicable for odd or even number N of array elements and the numbering of elements starts from the right side of the array.

4.2 Wave radiation to the near field

Supplementary Figure 4 presents a comparison of near field wave radiation from the focused phased array and folded tessellated array. In all cases, the focusing is targeted to the broadside location $\beta = 0°$. The acoustic pressure shown in the sub-figures of Supplementary Figure 4 is normalized to the maximum value of $N = 32$ in the corresponding row. In the top row, the driving frequency is 1 MHz, as in Fig. 3a,b,c of the main text, although the focal length $F = 64\lambda$ which is double the value in Fig. 3a,b,c (32λ). The focal length in the middle row of Supplementary Fig. 4 is $F = 32\lambda$ for 1 MHz excitation, while the normalized value $F / \lambda = 64$ due to the increase of the frequency to 2 MHz. In the bottom row, the normalized focal length is $F / \lambda = 128$. The number of transducer elements N is increased from left to right in each row while the array length is constant. The visualization convention used in Fig. 3 that shows the phased array results on the left half of each sub-figure and tessellated array results on the right half is likewise used in Supplementary Figure 4. Similarly, a black dot is placed between both halves of the sub-figure to denote the ideal focal point.

For $N = 4$ in Supplementary Fig. 4(a), the degraded capability of the phased array to focus energy is observed since there is no location at broadside where a notable focusing effect occurs. Also, considerable sidelobes of large normalized acoustic pressure are observed, which contradicts the aim of focusing acoustic energy. In contrast, the tessellated array shows better focusing capability with concentrated energy at broadside using $N = 4$ transducer constituents. The significance of the sidelobes are also suppressed by the tessellated array. Viewing the top row from left to right, the focusing provided by the phased array is gradually enhanced with the increase of transducer elements. For the tessellated array, the relative improvement in focusing for increasing number of constituents (viewing the top row from left to right) is not as great for the phased array because the focusing capability is already considerable with just $N = 4$ elements. When the number of transducer elements is increased to $N = 16$, the phased array nearly converges to the wave radiation characteristics of the tessellated array. Considering the middle row in Supplementary Fig. 4, the phenomena described above are also replicated although the focusing capability of the phased array with $N = 4$ elements in Supplementary Fig. 4(e) is notably poor when compared to the tessellated array. Another distinction is found. It is seen that the convergence of phased array and tessellated array does not occur for $N = 16$ in Supplementary Fig. 4(g) with the 2 MHz wave. Instead, $N = 32$ transducer elements, Supplementary Fig. 4(h), lead to a more complete similarity between the phased and tessellated arrays. This is because for the phased array an increased number of transducer elements is needed to provide for similar focusing effectiveness when the driving frequency increases and focal point draws nearer to the array [10].

The arrays in the bottom row of Supplementary Fig. 4 are intended to focus energy at the same location with the top row, using a frequency that is twice (2 MHz) that used in the top row (1 MHz). Considering the phased array in the bottom row, it is seen that the energy focusing trend at 2 MHz approximately converges to the tessellated array wave radiation trends for $N = 32$ in Supplementary Fig. 4(l). Indeed, for $N = 16$, the phased array still show signs of noticeable sidelobes in Supplementary Fig. 4(k). As a

comparison, there is almost no difference between phased arrays of $N = 16$ and $N = 32$ in the top row. For the discrete system of N transducer elements, the computed time difference from Eq. (25) has discrepancies respecting the ideal continuous parabolic delay. For greater frequency, phase differences caused by the same time delay are larger. In other words, the original discrepancies between the phased array and tessellated array towards focusing at $F = 64\lambda$ at 1 MHz in the top row of Supplementary Fig. 4 are exacerbated as seen in the bottom row results of Supplementary Fig. 4 where the corresponding values are $F = 128\lambda$ at 2 MHz driving frequency. Thus, the phased array is more challenged to focus at higher frequencies when compared to the focusing properties of the tessellated array of the same N constituents. For 2 MHz excitation, the tessellated array of $N = 8$ elements exhibits nearly equivalent wave focusing as the tessellated array with $N = 32$ elements. This indicates that the tessellated array exhibits less sensitivity of wave radiation properties than the phased array for changing number of transducer elements, and may provide greater wave focusing for few elements than the phased array. The influence of focal length is reflected by the comparison of Fig. 3 with the top row of Supplementary Fig. 4. For $N = 8$, the focusing behavior of the phased array is closer to the tessellated array in Supplementary Fig. 4(b) than Fig. 3(b). This is because the more distant focal point provides a general challenge to the aim of focusing acoustic waves, so as to lessen the significance of ideally reconstructing a continuous parabolic time delay through a spatially sampled representation.

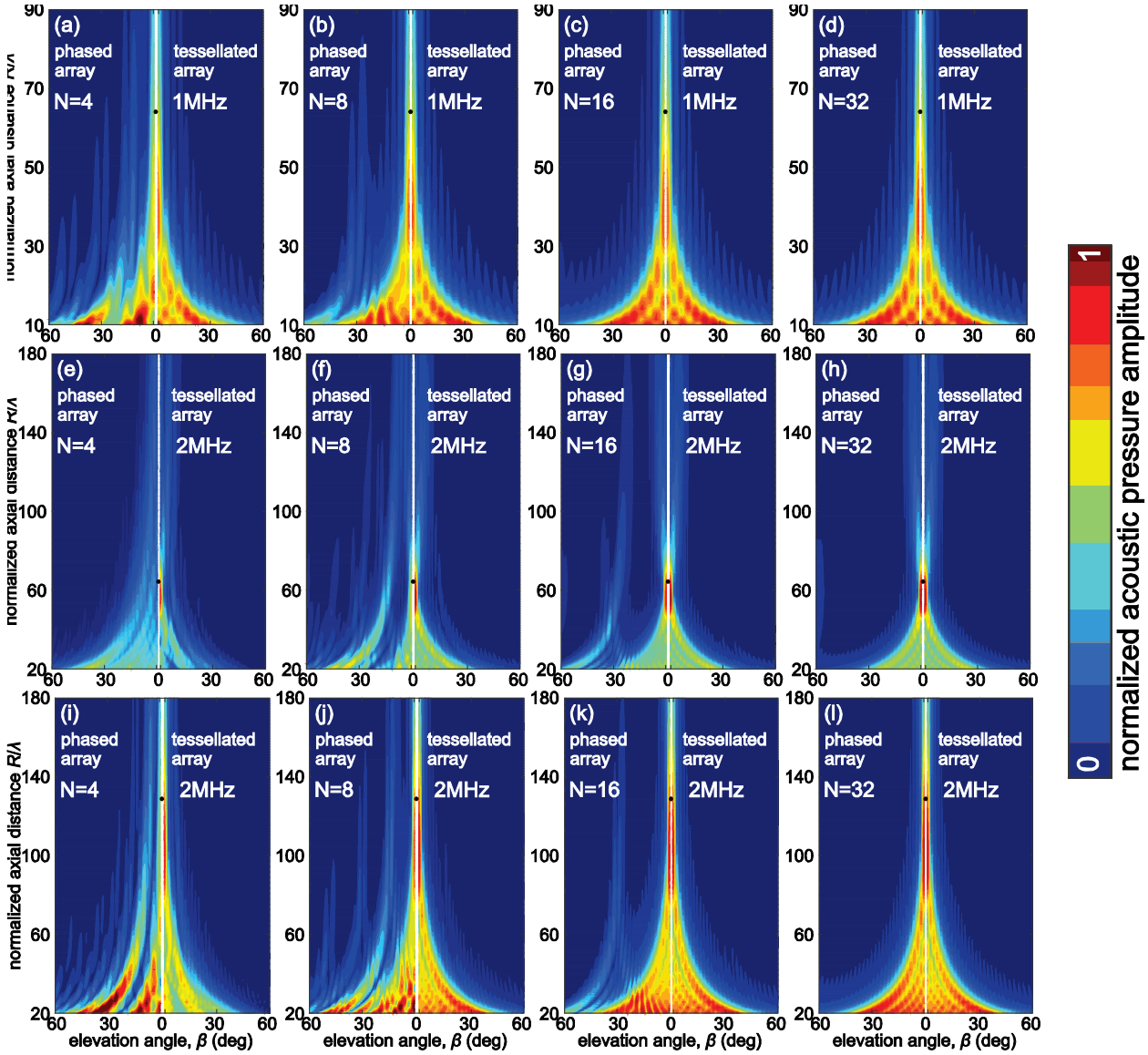

Supplementary Figure 4. Near field normalized acoustic pressure as a function of elevation angle β and normalized axial distance R/λ at azimuth angle $\phi = 0°$. Each plot contrasts the phased array (left) with tessellated array (right), and the middle strip is intentionally left blank for ease of visualization, wherein the black dot refers to the location of designed focal point. The number of transducer elements N is increased from left to right in each row, and the acoustic pressure is normalized by the maximum value in corresponding $N = 32$.

4.3 Wave radiation to the far field

Then the contrasts between phased array and tessellated array are investigated beyond the transition distance, i.e. into the far field, in Supplementary Fig. 5. The driving frequency in the top row is 1 MHz while 2 MHz for the bottom. The left-most column contrasts the directivity of focused (quadrants 1 and 2) and unfocused (quadrants 3 and 4) cases for $N = 16$ (quadrants 1 and 3) and $N = 32$ (quadrants 2 and 4). The right two columns present the directivity contrast under different focal lengths, and each plot includes

the results of different transducer elements (1st quadrant $N = 4$, 2nd quadrant $N = 8$, 3rd quadrant $N = 16$, and 4th quadrant $N = 32$).

For the unfocused case in Supplementary Fig. 5(a) (quadrants 3 and 4), the directivities of both arrays are nearly the same for $N = 16$ and $N = 32$ numbers of constituents. Once both arrays are focused at $F = 32\lambda$ (quadrants 1 and 2), although minor distinctions exist for $N = 32$ elements (quadrant 2) due to the convergence of phased array, significant differences in directivities appear for $N = 16$ (quadrant 1). The magnitudes of the sidelobes of phased array become larger than phased array across the elevation angle range β =[40°, 80°] . This reveals the tessellated array is better at reducing the sidelobes, which can avoid the potential negative influences on broadside focusing. Considering tessellated arrays of different refined levels in Supplementary Fig. 5(b, c, e, f) as observed for the four quadrants (N =4, 8, 16, 32) in each sub-figure, there is little difference among the far field wave radiation patterns. This means that focused tessellated arrays may be only slightly influenced in terms of far field wave radiation properties for different numbers of transducer elements N . In contrast, as shown throughout Supplementary Fig. 5, the directivities of the phased array change are much more strongly influenced by changing number of transducer elements. Additionally, the sidelobe SPL for the tessellated arrays are rarely greater than for the phased array.

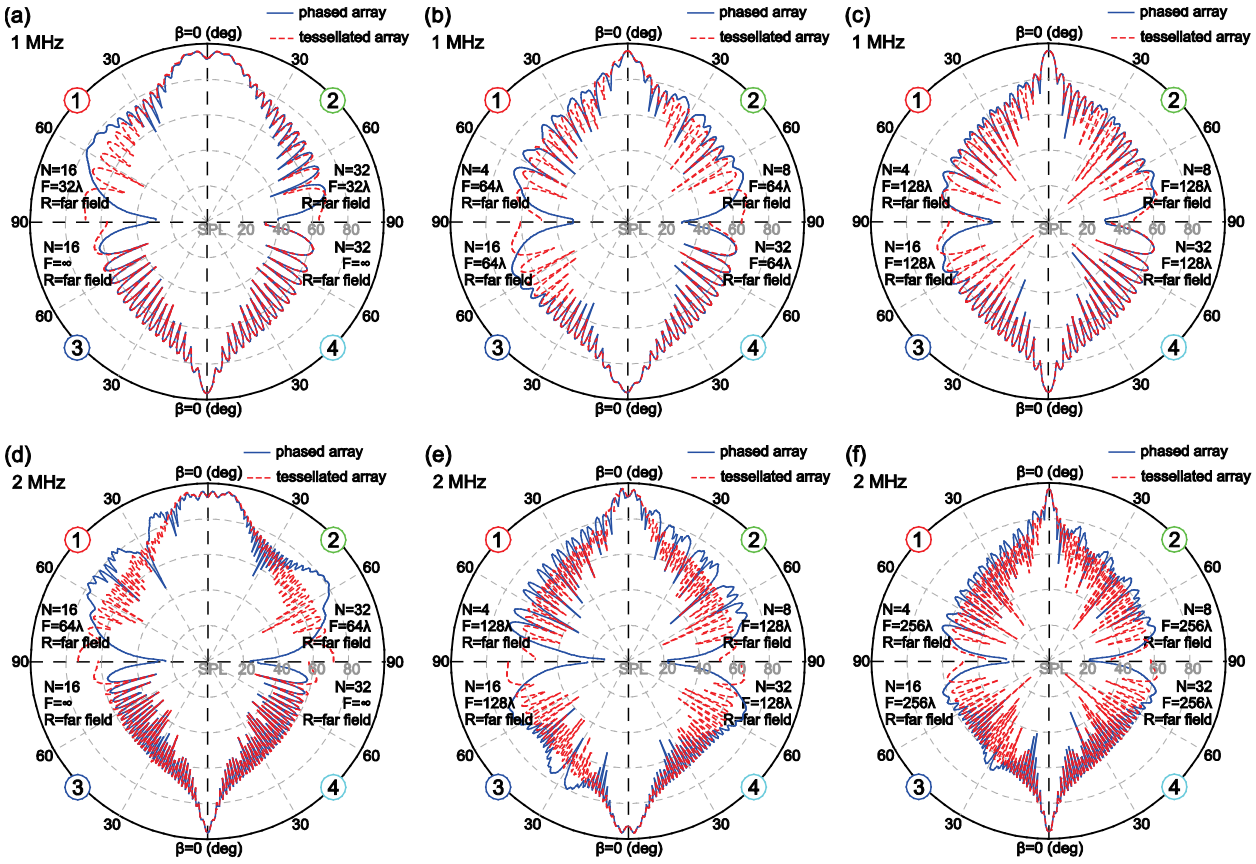

Supplementary Figure 5. Far field sound pressure level (SPL) as a function of elevation angle β at azimuth angle ϕ = 0°. Each quadrant contrasts the phased array (solid blue) with tessellated array (dashed red). (a) and (d) present the directivities of focused and unfocused arrays for $N = 16$ and $N = 32$. In (b), (c), (e), and (f), each plot demonstrates the

directivity of focused arrays with different transducer elements (1st quadrant $N = 4$, 2nd quadrant $N = 8$, 3rd quadrant $N = 16$, and 4th quadrant $N = 32$). The driving frequencies are 1 MHz (top row) and 2 MHz (bottom row).

5 Contrast between tessellated array and classical arc radiator

5.1 Acoustic pressure radiated from classical arc radiator

The ideal arc wave radiator is shown in Supplementary Fig. 6. The arc width is considered to be the same as the constituent dimension d so that the arc and tessellated arrays possess the same area of transduction and thus the same global means for wave radiation. Here the classical arc radiator surface is discretized by triangular elements. Then, Rayleigh's integral is evaluated over each discretized sub-area with the superposed results from all sub-areas used to predict the acoustic field at near and far field locations. The discretization of the arc is sufficient fine so that the nearest location considered remains in the acoustic far field of all sub-areas.

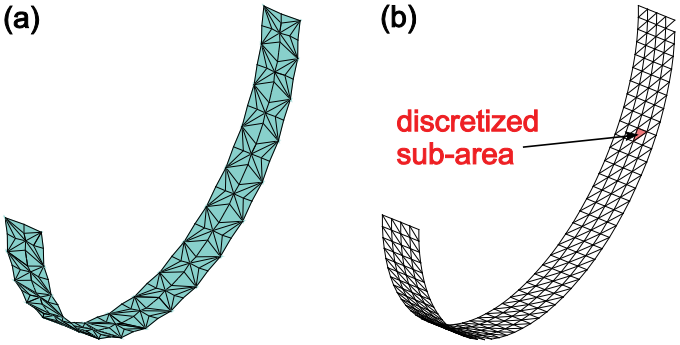

Supplementary Figure 6. (a) Folded tessellated array of $N = 16$. (b) The corresponding ideal arc of the tessellated array shown in (a). The discretization is refined sufficiently in the computation of Rayleigh's integral, while the coarse discretization is for ease of visualization here.

5.2 Wave radiation to the near field

The near field comparisons of the tessellated array and classical arc radiator are explored in Supplementary Fig. 7. The driving frequencies are 2 MHz and 3 MHz in the top and bottom rows, respectively. Each row includes the results of foldable, tessellated arrays (N = 4, 8, and 16) and arc radiator. For each row, the normalized acoustic pressure is taken with respect to the maximum of the row, which occurs for the arc radiator. It is worth noting that the ranges of radial distance and curvature radius in Supplementary Fig. 7 are the same with Fig. 4, although the axes ticks are distinct due to the wavelength normalization.

For $N = 4$ in Supplementary Fig. 7(a), the coincidence of geometric focal length and focused acoustic energy indicates that the acoustic pressure is governed by folding-induced curvature. Yet, compared with the same topological configuration in Fig. 4a, the focused acoustic energy is not of high intensity, which is caused by the increased frequency. The geometric discrepancies between the tessellated array and ideal arc are the same for Fig. 4a and Supplementary Fig. 7(a), although for the 2 MHz driving frequencies there is less respective similarity among the resulting wave focusing capabilities. This distinction is caused by the the approximation of the arc geometry by a tessellated surface, which is acoustically less effective when

the wavelengths are smaller. Extending this assessment, the energy focusing of the tessellated array of N =4 transducer elements in Supplementary Fig. 7(e) is reduced further when compared to the corresponding idea arc. Yet, for sufficient refinement of the tessellated array, viewing the Supplementary Fig. 7 from left to right shows that the refined tessellated structure trends to the similar wave radiation properties as the ideal arc of the same array length.

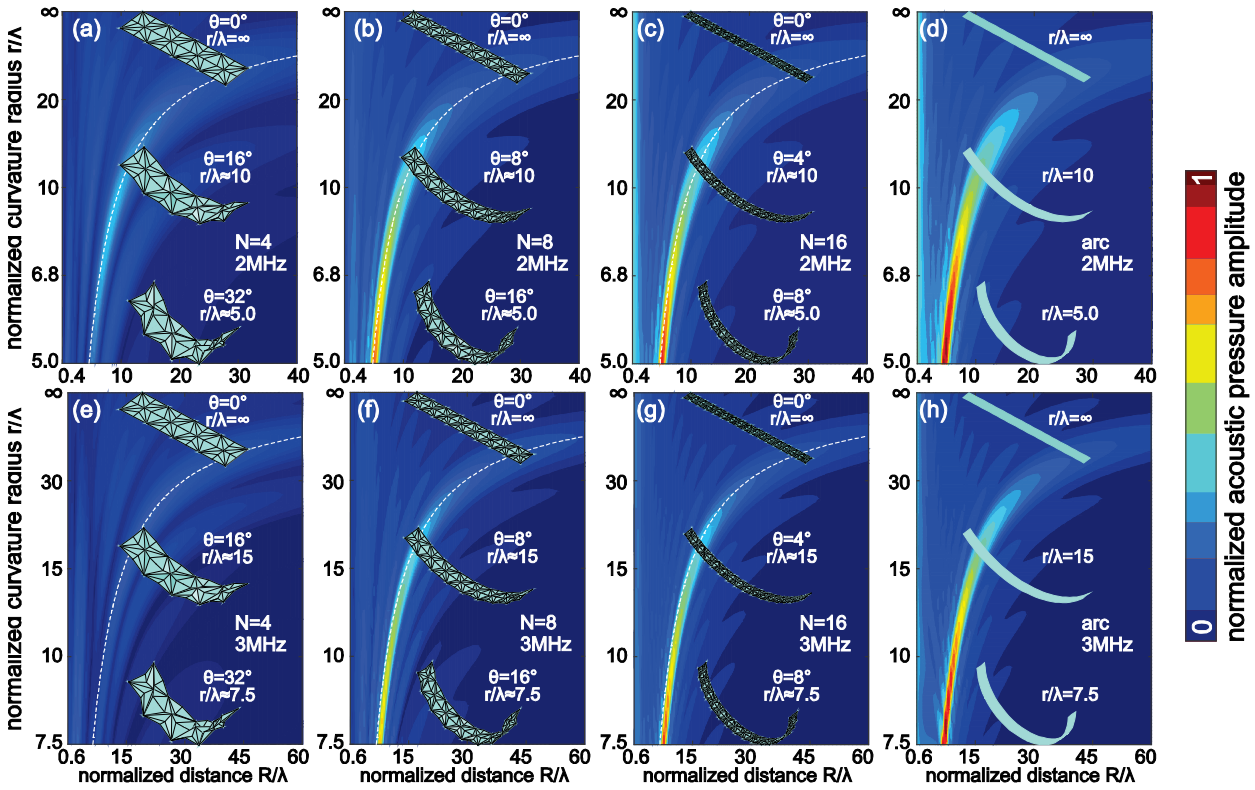

Supplementary Figure 7. Near field normalized acoustic pressure at broadside as a function of normalized axial distance R/λ and normalized curvature radius r/λ. The acoustic radiators are tessellated transducer array $N = 4$ (a, e), $N = 8$ (b, f), $N = 16$ (c, g), and arc radiator (d, h), respectively, and the increase of N refines the tessellated array to approach the target arc. The acoustic pressure in each row is normalized by the maximum value in corresponding arc. The dashed white line plots the geometric focal length of the curved tessellated array. The driving frequencies are 2 MHz (top row) and 3 MHz (bottom row).

5.3 Wave radiation to the far field

Comparisons between the refined tessellated array and classical arc radiator are provided in Supplementary Fig. 8 for far field radiation, considering either focused/folded or unfocused/unfolded array configurations. In each plot, the tessellated arrays of different refinement levels (1st quadrant $N = 4$, 2nd quadrant $N = 8$, and 3rd quadrant $N = 16$) are compared to the arc in the 4th quadrant. From left to right in columns, the tessellated arrays are folded to achieve the approximation of half, quarter, and eighth of circular sources, respectively. The driving frequencies are 30 kHz and 40 kHz for the top and bottom rows, respectively.

Considering Supplementary Fig. 8(a), the folded arrays are refined to radiate sound like a half circle source under 30 kHz excitation. For $N = 4$ in the 1st quadrant, there are multiple deep nodes and the radiated

response is very directive, which results from the local shape change of constituents. With the increase of the number of constituents to $N = 8$, the more accurately reconstructed and smoother curvature of the tessellated array results in more uniform directivity of the SPL. As a result, the depths of the nodes are reduced in the 2nd quadrant of Supplementary Fig. 8(a). Yet, this refinement extent is not sufficient for 40 kHz in Supplementary Fig. 8(d) since deep nodes remain for $N = 8$. The further refinement of the tessellated array with $N = 16$ constituents in the 3rd quadrant of Supplementary Fig. 8(d) results in a far field response more comparable to the half circle arc radiator for $\beta \in [0°, 90°]$, which substantiates the prior argument. Supplementary Fig. 8(b) and (e) present the results of the tessellated array and arc radiator that conform to a quarter circle radius of curvature. An elevation angle range of more uniform response is observed from about [0°, 40°] for the arc. The SPL decreases promptly with further increase in elevation angle because the normal vectors of the sources do not project over these regions, which explains why the directivity is not uniform in this angular range as well. The good agreement between refined tessellated array and limiting case is also captured, such as $N = 16$ for 40 kHz driving frequency in Supplementary Fig. 8(e). For the wave radiators that conform to one-eighth of a circle as shown in Supplementary Fig. 8(c) and (f), the covered range of uniform directivity is further narrowed to $\beta \in [0°, 20°]$. By the refinement of the tessellated array, at either 30 or 40 kHz excitation, the resulting far field beam pattern begins to effectively approach the same beam pattern of the counterpart arc source that is of the same length.

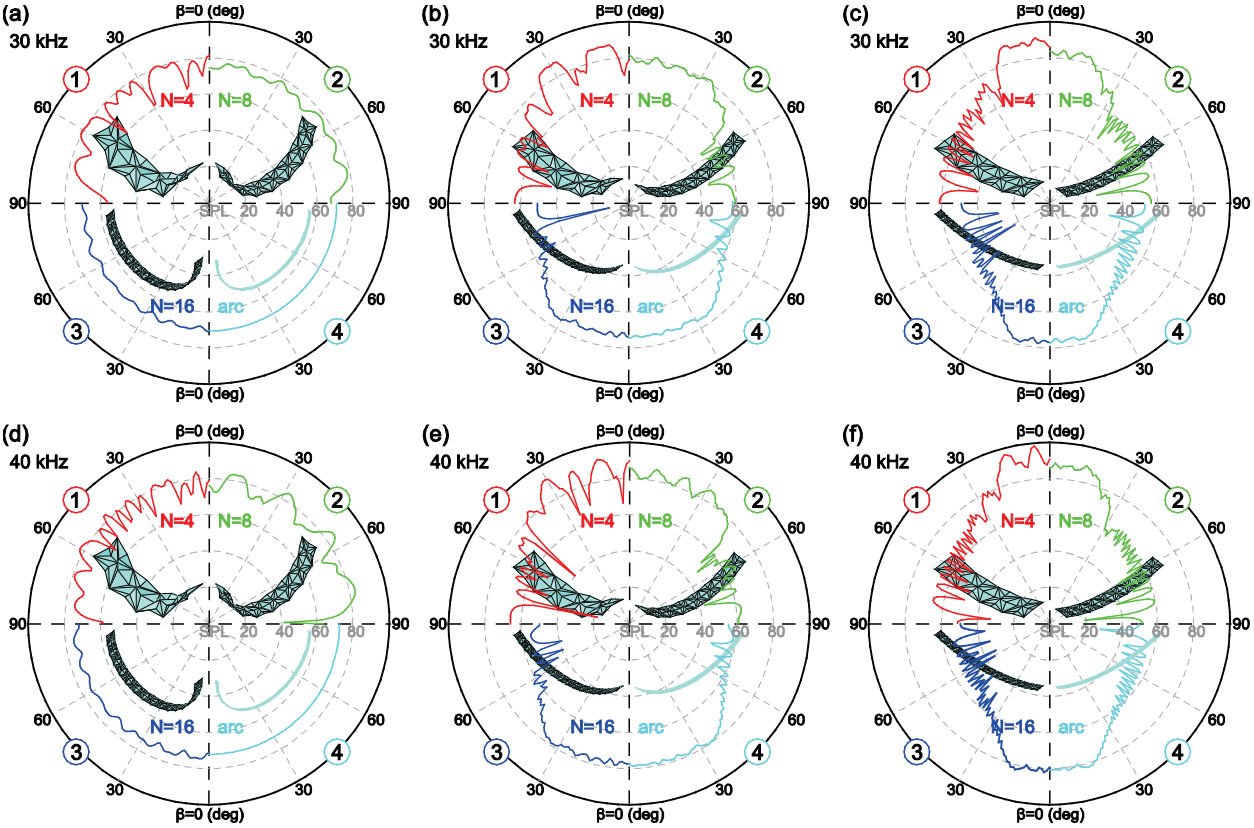

Supplementary Figure 8. Far field sound pressure level (SPL) as a function of elevation angle β at azimuth angle $\phi = 0°$. Each plot compares the tessellated arrays of different refinements (1st quadrant $N = 4$, 2nd quadrant $N = 8$, and 3rd

quadrant N = 16) with the limiting arc radiator (4th quadrant). The folded tessellated arrays or the arc are half (a, d), quarter (b, e), and eighth (c, f) of corresponding circle. The driving frequencies are 30 kHz (top row) and 40 kHz (bottom row).

References

[1] L.E. Kinsler, A.R. Frey, A.B. Coppens, and J.V. Sanders, *Fundamentals of Acoustics* (John Wiley and Sons, New York, 2000).

[2] D.A. Bies and C.H. Hansen, *Engineering Noise Control: Theory and Practice* (Spon Press, London, 2006).

[3] C. Zou and R.L. Harne, Adaptive acoustic energy delivery to near and far fields using foldable, tessellated star transducers, Smart Mat. Struct. **26**, 055021 (2017).

[4] J.M. Gattas, W. Wu, and Z. You, Miura-base rigid origami: parameterizations of first-level derivative and piecewise geometries, J. Mech. Des. **135**, 111011 (2013).

[5] M. Schenk and S.D. Guest, Geometry of Miura-folded metamaterials, Proc. Natl. Acad. Sci. U.S.A. **110**, 3276-3281 (2013).

[6] L. Josefsson and P. Persson, *Conformal array antenna theory and design* (John Wiley and Sons, New Jersey, 2006).

[7] K.B. Ocheltree and L.A. Frizzell, Sound field calculation for rectangular sources, IEEE Trans. Ultra. Ferro. Freq. Ctrl. **36**, 242-248 (1989).

[8] E.G. Williams, *Fourier Acoustics: Sound Radiation and Nearfield Acoustical Holography* (Academic Press, San Diego, 1999).

[9] L. Azar, Y. Shi, and S.C. Wooh, Beam focusing behavior of linear phased arrays, NDT & E Intl. **33**, 189-198 (2000).

[10] O.T. Von Ramm and S.W. Smith, Beam steering with linear arrays, IEEE Trans. Biomed. Eng. **8**, 438-452 (1983).